JMEPEG (2015) 24:2451–2463
DOI: 10.1007/s11665-015-1481-6

©ASM International
1059-9495/$19.00

On the Specific Role of Microstructure in Governing Cyclic Fatigue, Deformation, and Fracture Behavior of a High-Strength Alloy Steel

K. Manigandan and T.S. Srivatsan

(Submitted January 14, 2015; in revised form March 10, 2015; published online April 18, 2015)

In this paper, the results of an experimental study that focused on evaluating the conjoint influence of microstructure and test specimen orientation on fully reversed strain-controlled fatigue behavior of the high alloy steel X2M are presented and discussed. The cyclic stress response of this high-strength alloy steel revealed initial hardening during the first few cycles followed by gradual softening for most of fatigue life. Cyclic strain resistance exhibited a linear trend for the variation of elastic strain amplitude with reversals to failure, and plastic strain amplitude with reversals to failure. Fracture morphology was the same at the macroscopic level over the entire range of cyclic strain amplitudes examined. However, at the fine microscopic level, the alloy steel revealed fracture to be essentially ductile with features reminiscent of predominantly "locally" ductile and isolated brittle mechanisms. The mechanisms governing stress response at the fine microscopic level, fatigue life, and final fracture behavior are presented and discussed in light of the mutually interactive influences of intrinsic microstructural effects, deformation characteristics of the microstructural constituents during fully reversed strain cycling, cyclic strain amplitude, and resultant response stress.

Keywords alloy steel, cyclic strain amplitude, fatigue life and fracture, microstructure, orientation, stress response

1. Introduction

A viable approach that has both gained increased attention and use in the materials industry in more recent years is to effectively compromise strength over ductility, or alternatively building a perfect balance between the two. This is exactly what manufacturers of metals, alloys, and their composite counterparts have been trying to achieve for the last three decades, i.e., since the early 1970s (Ref 1-4). With specific reference to metals, such as high-strength steels, the mechanical properties to include fracture toughness are often governed by the independent or conjoint influences of the following: (a) chemical composition, (b) processing history and development of intrinsic microstructural features, (c) geometry or part thickness, (d) temperature of operation, (e) loading-rate, and (f) the presence of constraints at the crack (flaw) tip (Ref 5-11). Conditions that tend to minimize constraints in a structure are almost always beneficial for enhancing the ability of a metal to deform plastically. This facilitates in improving the fracture toughness, cyclic fatigue resistance, and overall damage tolerance capability of the high-strength steel (Ref 12-18).

A minor modification in chemical composition of the hot-worked die steel (AISI designation: H-12) by way of reduction in carbon content to 0.15% coupled with carburization resulted in a steel that was named as X2M and marketed to potential end-users under the trade name Vasco X2M. The carburized Vasco X2M was initially used for high-performance gears that were put to use for the helicopters of the U.S. Army (Ref 19, 20). Besides, this steel was also being chosen for use in other U.S. Army rotor craft power train components. Selection and use of this steel for such performance-critical components necessitated the need to evaluate the synergistic influence of composition, processing, and microstructure on response of this material to both static and dynamic loading. In the preliminary days, manufacturers of this high-strength specialty steel found it difficult to carburize when compared to companion steels on account of the tendency to easily form carbide particles on the surface. An aspect was initially shown in the published literature by Cunningham (Ref 19, 20). Sustained research and development efforts did eventually lead to successful carburization coupled with a good concentration of carbon (Ref 21).

In an earlier study, Averbach and coworkers (Ref 22) attempted to systematically document the growth rates of fatigue cracks propagating through both the case and into the core for carburized X2M steel. In their study, the fatigue cracks were propagated at constant stress intensities (ΔK) and also at a constant cyclic peak load, and the crack growth rates were observed to pass through a minimum value as the crack traversed the carburized case. The observed reduction in crack propagation rates was ascribed to be due to compressive stresses, which were developed in the case. Their study did reveal an overall good combination of resistance to simple crack initiation in the case, and fracture toughness in the core could be achieved in steel X2M, thereby suggesting that the material would be a viable candidate for use in heavy duty gears, and in gas turbine main-shaft bearings. In a subsequent and more recent study on the high cycle fatigue behavior of high-strength alloy steel, Davies and Jenkins (Ref 23) examined the high cycle fatigue behavior under conditions similar to

K. Manigandan and **T.S. Srivatsan,** Division of Materials Science and Engineering, Department of Mechanical Engineering, The University of Akron, Akron, OH 44325-3903. Contact e-mail: tsrivatsan@uakron.edu.

those encountered at the tooth root of helicopter gears. Their fatigue test results revealed crack initiation to occur either within the case or the core. The propensity for nucleation to occur at either site was strongly dependent on applied stress. However, when the same steel was tested at 150 °C in oil, it did exhibit a noticeable degree of mean stress sensitivity causing the fatigue endurance to decline, generally in the form of a straight line, as the load ratio became more positive. In essence, by raising the test temperature from 27 to 150 °C, the fatigue endurance was observed to decline. The authors attributed to the observed reduction in cyclic fatigue life to be primarily due to two competing factors: (i) a relaxation of the shot peened surface as a consequence of thermal stress relief, and (ii) easier movement of dislocations at the elevated temperature.

In this paper, we present and discuss the results of a recent study aimed at understanding the influence of test specimen orientation and intrinsic microstructural effects on cyclic strain amplitude-controlled response, fatigue life, and final fracture behavior of the high alloy content steel X2M. The underlying mechanisms governing (a) cyclic stress response, (b) cyclic strain resistance and resultant fatigue life, and (c) final fracture behavior are discussed in light of the conjoint and mutually interactive influences of intrinsic microstructural effects, magnitude of cyclic strain amplitude and resultant response stress, test specimen orientation, deformation characteristics of the microstructural constituents, and fatigue life.

2. Material

The high alloy steel, denoted as X2M, has a chemical composition (in wt.%) of 0.14 carbon, 0.50 manganese, 1.34 tungsten, 5.0 chromium, 1.4 molybdenum, and 0.5 vanadium. The steel was produced using a combination of vacuum induction melting and vacuum arc re-melting (VIM-VAR) by Teledyne Vasco. The presence of carbon provides solid solution strengthening while concurrently enabling a noticeable enhancement in hardenability through the formation and presence of carbide particles in the microstructure. The carbide particles contribute to the overall strength to this steel. The presence of chromium (Cr: 5%), molybdenum (Mo: 1.4%), tungsten (W: 1.34%), and vanadium (V: 0.5%) results in the formation and presence of a noticeable quantity of carbide particles, which contributes, either directly or indirectly, to increasing the strength of the steel matrix. Typically, this alloy steel is carburized in an atmosphere of nitrogen-methanol natural gas at 955 °C [1750 °F] and controlled by means of an oxygen-level probe. In striving to keep pace with the demands posed by emerging technological innovations, the technique of vacuum carburizing has emerged as a viable and attractive alternative to traditional carburizing. The alloy steel VascoX2M that was characterized in this study is the non-carburized base metal, representing the tough and fatigue resistant core, which has a healthy dispersion of carbide particles.

3. Experimental Procedures

3.1 Preparation of Test Specimen

Cylindrical test specimens, conforming to specifications outlined in ASTM E8-13 (American Society for Testing Material, 2013), were precision machined from the chosen steel (Ref 24). The length-to-diameter ratio of the fatigue test specimen was chosen to ensure that it would not buckle under fully reversed total strain amplitude-controlled cyclic deformation. To minimize the effects and/or contributions arising from surface irregularities and finish, final preparation of the test specimen surface was achieved by mechanically polishing the gage section of all test specimens to remove any and all circumferential scratches and surface machining marks.

3.2 Microstructural Characterization

Samples of the steel, taken from both the longitudinal (L) and transverse (T) orientations, were prepared in conformance with standard procedures used for the metallographic preparation of metal samples. The as-polished samples were then etched using nital reagent, i.e., a solution mixture of nitric acid (HNO_3) in methanol (CH_3OH). The polished and etched samples were examined in an optical microscope, at low magnifications, and photographed using standard bright field illumination technique.

3.3 Indentation Hardness

3.3.1 Microhardness Measurement. The value of hardness provides a measure of the resistance of this hard material to deformation, densification, and cracking or fracture (Ref 25-27). The Vickers microhardness [H_v] of the chosen alloy steel sample was measured using a Microhardness tester [Model: INSTRON Wilson Tukon 2100]. The machine makes an indent or impression on the polished surface of the alloy steel sample. The length of the projected diagonals of each indent or impression on the polished surface of the sample was carefully measured using the attached optical microscope. The Vickers microhardness was calculated from the ratio of applied load to the contact area enclosed within the four faces of the undeformed indenter.

The indentation load used was 500 g (4.9 N) for a dwell time of 15 s. Five indents were made across the polished surface of the chosen alloy steel sample, and the result reported is the average value in units of Kg/mm^2 and GPa.

The macrohardness measurements (R_B) were made on a Rockwell hardness machine using an indentation load of 100 Kgf, a minor load of 10 Kgf, and a 1/16th inch steel ball, a dwell time of 10 s and the value read on the 'B' scale. The macrohardness tests were also done on the polished surface of the alloy steel test specimen. The two chosen samples of the alloy steel, i.e., Sample # Longitudinal and Sample # Transverse, were examined for both microhardness and macrohardness measurements. The results of the microhardness and macrohardness measurements are summarized in Table 1.

3.4 Mechanical Testing (Tension plus Fatigue)

Uniaxial tensile tests were performed up until failure on a fully automated, closed-loop servohydraulic mechanical test machine [INSTRON Model 8500 plus] equipped with a 10,000 Kg (98 KN) load cell. The test specimens were deformed at a constant strain rate of 0.0001/s. An axial 12.5-mm gage length extensometer was attached to the test specimen at the gage section, using rubber bands, to provide a precise measurement of strain during uniaxial loading and resultant stretching of the test specimen. The stress and strain measurements, parallel to the load line, were recorded on a PC-based data acquisition system (DAS).

Table 1 A compilation of the microhardness and macrohardness of the high alloy steel in the two orientations

	Macrohardness (average)		Microhardness (average)	
Steel	**HR_B**	**MPa**	**H_V**	**MPa**
X-2M longitudinal orientation	85	565	299	986
X-2M transverse orientation	86	570	398	1263

The cyclic strain-controlled fatigue tests were also performed on a fully automated closed-loop servohydraulic structural test machine. The tests were conducted in the axial total strain amplitude control mode under fully reversed, push-pull, tension-compression loading. For each individual test, the test machine was programmed to maintain a constant nominal strain rate of 0.001/s. The test common signal (strain function) was a triangular waveform, and the mean strain was zero. All total strain amplitude-controlled ($\Delta\varepsilon_T/2$) cyclic fatigue tests were initiated in tension. An axial 12.7-mm clip-on extensometer was attached to the test specimen at the gage section, using rubber bands, for the purpose of monitoring total strain amplitude during fully reversed strain amplitude-controlled fatigue tests such that the magnitude of negative strain equals the magnitude of positive strain ($R_\varepsilon = \varepsilon_{\text{minimum}}/\varepsilon_{\text{maximum}} = -1$).The controlled variable is total strain amplitude, and the cyclic strain-controlled tests were performed over a range of total strain amplitudes ($\Delta\varepsilon_T/2$). The extensometer was calibrated prior to the initiation of each fatigue test. The test machine was checked for alignment prior to the start of every fully reversed strain-controlled low-cycle fatigue (LCF) test. The tests were conducted in laboratory air environment (temperature of 27 °C and relative humidity of 55%) at a frequency of one-hertz (1 Hz). The stress and strain data for each fatigue test were recorded on a PC-based DAS. The number of cycles-to-failure, or separation, is taken as fatigue life (N_f).

3.5 Failure-Damage Analysis

Fracture surfaces of the cyclically deformed and failed fatigue test specimens of this high alloy steel were comprehensively examined in a scanning electron microscope (SEM) to essentially determine the following:

(i) The macroscopic fracture mode, and to concurrently characterize the following:
(ii) The fine scale topography, the nature of crack initiation, the nature, extent and depth of early crack propagation, the extent and depth of stable crack propagation prior to the onset of unstable crack propagation, and
(iii) Other intrinsic features on the fracture surface.

All of these for the purpose of establishing the microscopic mechanisms contribute to failure by fracture.

The distinction between the macroscopic mode and microscopic fracture mechanisms is based entirely on the magnification level at which the observations were made. The macroscopic mode refers to the overall nature of failure, while the microscopic mechanisms relate to the "local" failure processes, to essentially include the following: (a) microscopic void formation and (b) microscopic void growth and eventual coalescence, the nature, intensity, and severity of the fine microscopic and macroscopic cracks dispersed through the fracture surface. The samples for observation in the SEM were obtained from the failed LCF specimens by sectioning parallel to the fracture surface.

4. Results and Discussion

4.1 Initial Microstructure

The microstructure of this high alloy steel sample is an important factor that essentially determines its hardness, tensile properties, cyclic fatigue resistance, and eventual fracture behavior. The optical microstructure of this high alloy steel in both the longitudinal (L) and transverse (T) orientations is shown in Fig. 1. The observed microstructure is quite typical of high-strength alloy steels in that it reveals at the fine microscopic level a combination of alloy-rich and alloy-depleted regions. Being a vacuum melt product, the amount of segregation, if any, on a gross scale is noticeably less than one would expect in an air melted and cast product. However, at the fine microscopic level, the segregation is still significant enough to have an impact on resistance to crack initiation. The "local" pockets of high carbon and high alloy content in this alloy steel resulted in the formation and presence of a noticeable volume fraction of martensite in these regions. The overall morphology of martensite in the alloy-rich and carbon-rich regions was in the form of short and fine needle-like laths. The fine martensitic laths were intermingled with isolated pockets of the ferrite-rich region, i.e., the base material. The observation of martensite micro-constituent in the alloy-rich regions is governed by a synergism of both the chemical composition and processing technique used to engineer the starting material. This does exert an influence on the following: (i) 'local' hardness, (ii) global tensile response, (iii) response to fatigue loading, and even (iv) overall fracture behavior. In both the longitudinal (L) and transverse (T) samples, the volume fraction of the alloy-rich and carbon-rich regions was noticeably more than the alloy-depleted region. The presence and distribution of other coarse second-phase particles in the microstructure of this high alloy steel could not be easily identified at the allowable magnifications of the light optical microscope (i.e., 1000×). It is observed that the smaller second-phase particles tend to occur primarily in the matrix, i.e., alloy lean region, consistent with the fact that the alloy carbide particles deplete the surrounding matrix of alloy content.

4.2 Hardness

Vickers's microhardness measurements were made edge-to-edge across samples taken from both the longitudinal and transverse orientations. Five measurements were made at different locations on the polished surface to gather information

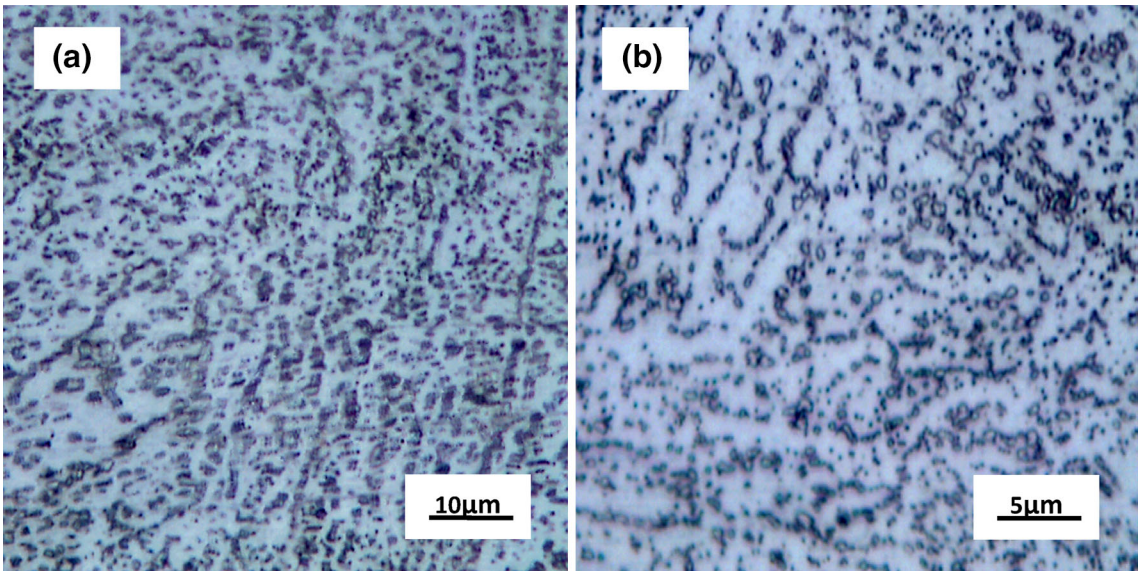

Fig. 1 Optical micrographs showing the key micro-constituents present in alloy steel X2M. (a) Longitudinal orientation, and (b) Transverse orientation

on spatial variability of hardness. The microhardness measurements provide useful information relevant to the intrinsic influence of size of the grains on strengthening and a concurrent weakening arising from the presence and distribution of processing-related defects, such as, (i) microscopic pores/voids, (ii) macroscopic pores/voids, (iii) their distribution through the microstructure, and even (iv) fine microscopic cracks. It is difficult to assess the exact magnitude of strengthening arising from the size and morphology of grains independent of the weakening effect. The microhardness measurement [resultant average value] in both the longitudinal orientation (986 MPa) and transverse orientation (1263 MPa) is summarized in Table 1.

The macrohardness measurements made from one edge to the other edge of the polished surface of the alloy steel sample and the average value are provided in Table 1. The average macrohardness of this alloy steel is 565 MPa in the longitudinal orientation and 570 MPa in the transverse orientation. The macrohardness values were fairly consistent across the width of the polished surface of the alloy steel specimen. For this high alloy steel, the noticeably lower value of macrohardness when compared one-on-one with the microhardness can be ascribed to the relative global nature of the macro-indent with the possibility of the presence of intrinsic microstructural defects, such as microscopic voids and fine microscopic cracks, contributing to the observed decrease in macrohardness when compared to the relatively 'localized' microhardness obtained from a simple micro-indent.

4.3 Tensile Properties

The tensile properties of the high alloy steel X2M, at ambient temperature (27 °C), are summarized in Table 2. Results reported are the mean values based on duplicate tests. The elastic modulus (E) of this high alloy steel was 175 GPa in the longitudinal (L) direction and 150 GPa in the transverse (T) direction. The transverse (T) direction shows a noticeable decrease of 14% in elastic modulus in comparison with the longitudinal (L) direction. This may have important implications relative to optimal orientation and machining of the test specimen. The yield strength of the X2M alloy steel in the longitudinal (L) direction [σ_{YS} = 371 MPa] was forty percent higher than the yield strength in the transverse (T) direction [σ_{YS} = 264 MPa]. The ultimate tensile strength in the longitudinal (L) direction [σ_{UTS} = 638 MPa] was observably twenty-two percent higher than the ultimate tensile strength in the transverse (T) direction [σ_{UTS} = 523 MPa]. This substantiates the strong dependence of properties on working direction coupled with distribution of second-phase particles in the microstructure and the resultant implications on processing of the final component of this steel. In both the longitudinal (L) and transverse (T) directions, the ultimate tensile strength (σ_{UTS}) is higher than the tensile yield strength (σ_{YS}) indicating the occurrence of noticeable strain hardening beyond yield. The ductility, quantified by elongation over 12.7 mm gage length, was 14% in the longitudinal (L) direction and 17 percent in the transverse (T) direction. The observed higher ductility in the transverse (T) direction is commensurate with the lower yield strength and tensile strength in this direction. The reduction in test specimen cross-section area, a direct measure of ductility, was 60% in the transverse (T) direction and 54% in the longitudinal (L) direction and reveals the same trend observed by the measurement of tensile elongation.

The engineering stress versus engineering strain curves for the two orientations are compared in Fig. 2. Both the longitudinal (L) and transverse (T) samples exhibit identical elastic behavior and near similar strain hardening characteristics. Immediately following the onset of necking, i.e., ultimate tensile strength, both the longitudinal (L) and transverse (T) samples of this high alloy steel exhibited substantial plastic deformation prior to failure by fracture.

4.4 Cyclic Strain Resistance or Low-Cycle Fatigue Properties

Cyclic plastic strain will tend to produce a number of damaging processes, which will tend to affect the microstructure of this high alloy steel, cyclic strain resistance, and

Table 2 A compilation of room temperature (T = 25 °C) tensile properties of alloy steel X-2M taken in both the longitudinal and transverse orientations (Results are mean values based on duplicate tests)

Orientation	Sample	Elastic modulus, GPa	Yield stress, MPa	Ultimate stress, MPa	Ductility, %	Reduction in area, %
Longitudinal	1	182	401	689	12.5	48
	2	168	341	587	16.1	60
	Mean	175	371	638	14.3	54.0
Transverse	1	162	295	544	16	54
	2	138	233	502	18.4	63
	Mean	150	264	523	17.2	60.0

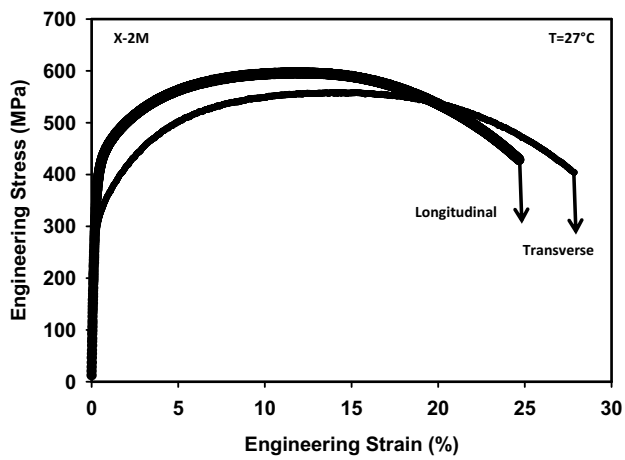

Fig. 2 Comparison of the engineering stress vs. engineering strain curves of alloy steel X2M for The two orientations: Longitudinal and Transverse when deformed at room temperature

resultant fatigue life (Ref 28-31). The early initiation and progressive growth of damage help relate the fatigue life (N_f) with cyclic strain amplitude [$\Delta\varepsilon/2$] during fully reversed [$R_\varepsilon = -1$] strain cycling. The empirical relationship between plastic strain amplitude [$\Delta\varepsilon_P/2$] and reversals to fatigue failure [$2N_f$], the Coffin-Manson relationship, was determined for the LCF regime [$N_f < 10^4$ cycles] and predicts that

$$[\Delta\varepsilon_P/2] = \varepsilon_f'[2N_f]^c \quad \text{(Eq 1)}$$

A best straight line fit for the plastic strain amplitude-reversals to fatigue life ($2N_f$) curve was obtained by linear regression analysis (Ref 26, 27). An extrapolation of the best fit is made to determine the value of cyclic plastic strain amplitude ($\Delta\varepsilon_P/2$) at 2 N_f = 1. This point in the plastic strain amplitude-fatigue life curve is the fatigue ductility coefficient [ε_f'] and can be related to cyclic ductility of the material. The slope of the plastic strain amplitude-reversals-to-fatigue life curve gives the fatigue ductility exponent, c.

The effect of fully reversed strain cycling on low-cycle fatigue response of this high alloy steel in both the longitudinal and transverse orientations is shown in Figure 3. Variation of cyclic strain amplitude [$\Delta\varepsilon/2$] with reversals to fatigue life [$2N_f$] curve can be viewed as an indication of the resistance offered by the microstructure of this high alloy steel to both crack initiation and failure. Throughout LCF testing of this high alloy steel, over the range of strain amplitudes studied, there was no evidence of the occurrence of specimen buckling. Based on width and height of the hysteresis loop for the different cycles, the plastic strain, elastic strain, and stress amplitude values

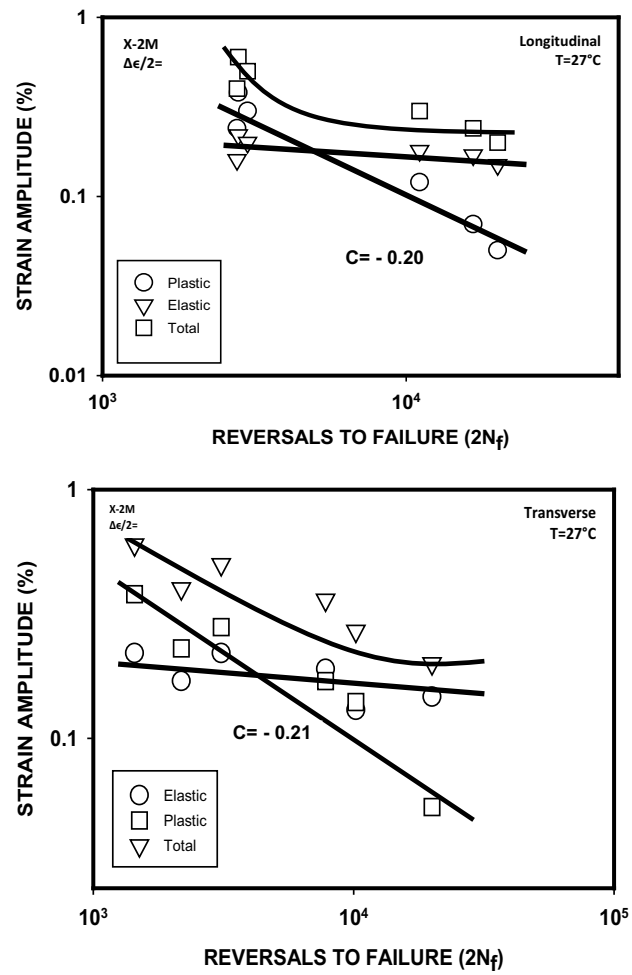

Fig. 3 Variation of cyclic strain amplitude ($\Delta\varepsilon/2$) with reversals-to-failure ($2N_f$) for alloy steel X2M at room temperature (27 °C). (a) Longitudinal orientation (b) Transverse orientation

were recorded by the control unit of the Instron servohydraulic test machine (Model 8500 Plus). For both the longitudinal (L) and transverse (T) orientations, variation of elastic strain amplitude [$\Delta\varepsilon_e/2$] with reversals-to-fatigue life [$2N_f$] is linear and the Basquin relationship is satisfied.

$$[\Delta\varepsilon_e/2] = \{\sigma_f'\}[2N_f]^b \quad \text{(Eq 2)}$$

Variation of plastic strain amplitude [$\Delta\varepsilon_P/2$] with reversals-to-fatigue life [$2N_f$] was also linear for both the longitudinal (L) and transverse (T) orientations, and the Coffin-Manson relationship is satisfied and can be used to determine the fatigue

behavior in the LCF regime [$N_f < 10^4$ cycles]. The value of fatigue ductility exponent [c] is −0.22 for the longitudinal (L) orientation and −0.23 for the transverse (T) orientation. This value is well within the generally observed range of 0.2 to 0.7 for most metals and their alloy counterparts (Ref 28-31).

4.5 Cumulative Glide and Cyclic Stress Response

The cyclic stress response curves or cumulative glide plots exemplify the variation of cyclic stress amplitude ($\Delta\sigma/2$) with cycles (N), at a fixed strain amplitude [$\Delta\varepsilon_T/2$], and provide a lucid illustration of the path taken by this high-strength alloy steel to its final level of stress during fully reversed total strain amplitude-controlled cyclic deformation. The curves also provide useful information pertaining to overall cyclic stability of the material. In a nutshell, the overall stability of the intrinsic microstructural features, during fully reversed strain cycling, coupled with an ability of the microstructure of this high alloy steel to distribute the plastic strain over the entire microstructural volume are two key factors that govern both stress response and fatigue life (N_f). The stress response curves for this alloy steel over the range of plastic strain amplitudes are shown in Fig. 4. Since plastic strain amplitude varied throughout testing, reaching a maximum value at the minimum stress and a minimum value at the maximum stress, the value at specimen half-life ($N_f/2$) is taken as the reference.

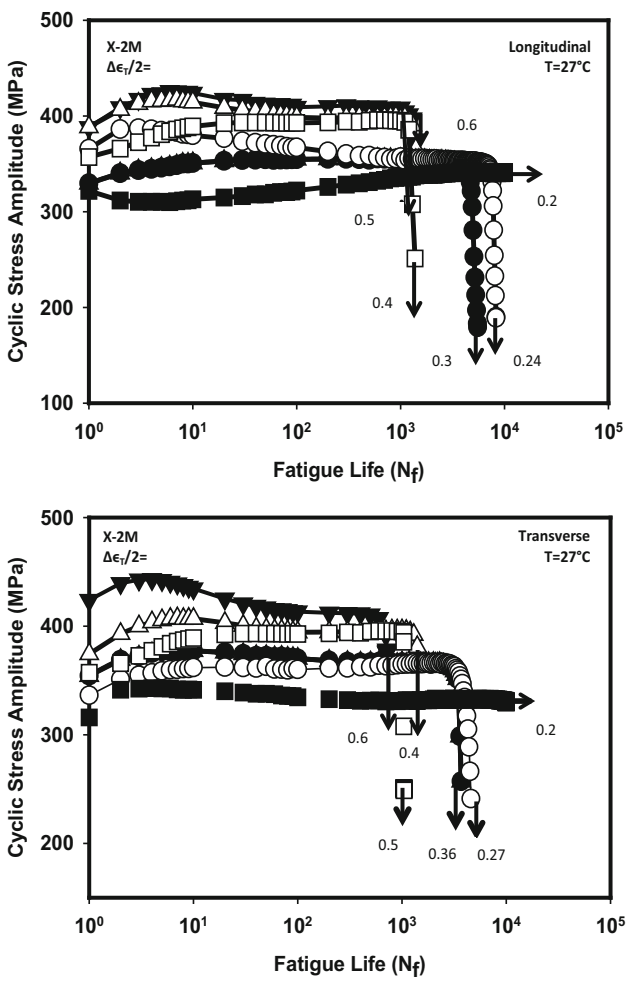

Fig. 4 Cyclic stress response curves for alloy steel X2M over the entire range of strain amplitudes, when deformed at room temperature (27 °C). (a) Longitudinal orientation, and (b) Transverse orientation

For both the longitudinal (L) and transverse (T) orientations, the response of this high alloy steel when cyclically deformed at low, intermediate, and high cyclic strain amplitudes showed evidence of initial hardening during the first few cycles of fully reversed straining. This was followed by gradual softening for most of fatigue life and culminating in rapid softening prior to failure by separation or fracture. Subsequent to initial hardening, the observed gradual decrease in stress-carrying capability of the microstructure of this high alloy steel can be ascribed to the following:

(i) The formation and presence of a number of fine microscopic cracks and their ensuing growth through the microstructure of this alloy steel during fully reversed cyclic straining.
(ii) Eventual coalescence of the growing microscopic cracks to form one or more macroscopic cracks.

The softening effect observed prior to failure is exacerbated by the concurrent growth of both the fine microscopic and macroscopic cracks through the microstructure of this high alloy steel. The softening effect, i.e., an observed decrease in stress response during fully reversed strain cycling, was more pronounced at the higher cyclic strain amplitudes and resultant short fatigue life.

The actual trend, i.e., hardening, softening, or stability, shown by the stress at the different strain amplitudes is better shown and analyzed by examining the variation of cyclic stress amplitude (MPa) with percent life (N/N_f) as is shown in Fig. 5. The curves in this figure clearly depict the trend shown by the stress at the different cyclic strain amplitudes. Variation of normalized stress (σ_N/σ_1) with cycles (N) is shown in Fig. 6, when the stress at any cycle (σ_N) is normalized with respect to the stress in the first cycle (σ_1), and provides a comprehensive overview of the degree of hardening or softening experienced by this alloy steel during fully reversed strain cycling. The observed degree of softening was noticeably greater at the higher cyclic strain amplitudes and resultant short fatigue life (N_f) than at the intermediate and lower cyclic strain amplitudes and resultant enhanced fatigue life (N_f). During fully reversed cyclic straining of this high-strength alloy steel, the progressive or gradual loss in strength arising from the conjoint and mutually interactive influences of (i) intrinsic microstructural changes, and (ii) the presence of fine microscopic and macroscopic cracks by far offsets the increased strength achieved through a combination of the following: (i) the presence of dislocations, (ii) a gradual increase in their number during repeated cyclic straining, (iii) the mutual interaction of dislocations with each other coupled with their interactions with other microstructural constituents in this alloy steel. The net result is rapid softening experienced by the microstructure of this high alloy steel immediately prior to catastrophic failure. For both the longitudinal (L) and transverse (T) orientations, the initial hardening followed by gradual softening at the chosen strain amplitude ($\Delta\varepsilon/2$) is identified by an initial increase and then gradual decrease of both the tensile and compressive stresses during fully reversed cyclic straining. This is shown in Fig. 7.

4.6 Mechanisms and Microscopic Mechanisms Governing Stress Response during Fully Reversed Cyclic Straining

In this alloy steel, as with other companion steels and ductile metals, the key mechanisms, which are likely to control the

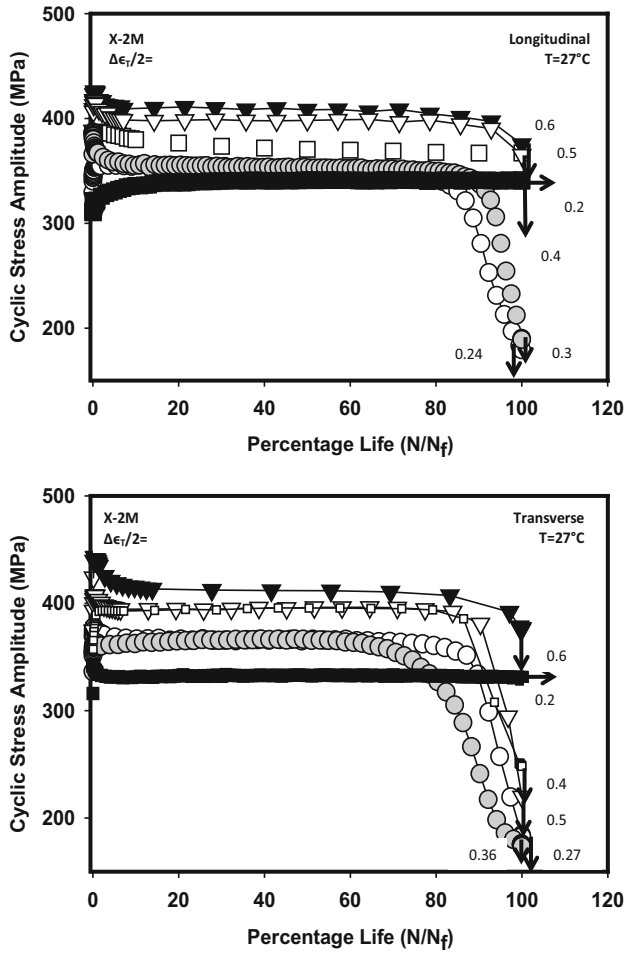

Fig. 5 Variation of cyclic stress amplitude (MPa) with percentage life (N/N_f) over the entire range of cyclic strain amplitudes investigated. (a) Longitudinal orientation, and (b) Transverse orientation

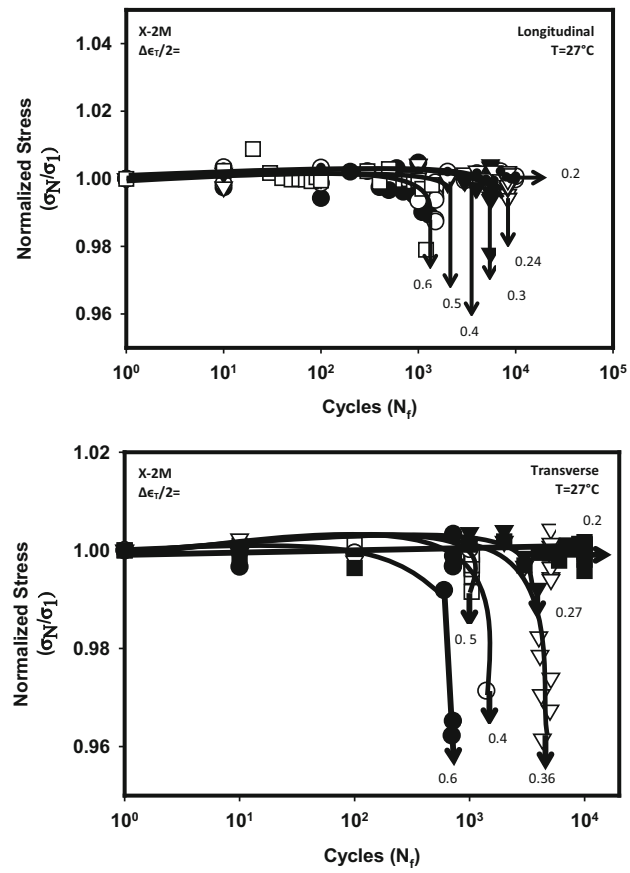

Fig. 6 Variation of normalized stress (σ_N/σ_1) with fatigue life (N_f) for alloy steel X2M when cyclically deformed at room temperature (27 °C). (a) Longitudinal orientation, and (b) Transverse orientation

variation of cyclic stress amplitude ($\Delta\sigma/2$) with cycles (N) during fully reversed strain cycling, are dependent on the mutually interactive influences of (i) microstructure of this high alloy steel, and (ii) cyclic strain amplitude [$\Delta\varepsilon/2$]. The most likely mechanisms governing stress response of this high-strength alloy steel X2M can be attributed to the mutually interactive influences of the following:

(a) An observable increase in the density of dislocations already present in the microstructure of this alloy steel, during cyclic deformation in the plastic range, by the process of dislocation multiplication.
(b) A gradual increase in the interaction of a moving or mobile dislocation with other dislocations.
(c) An interaction of the moving dislocations with the second-phase carbide particles dispersed through the microstructure coupled with the formation and presence of fine slip bands and their interaction upon impingement with the grain boundaries.

At the low and intermediate cyclic strain amplitudes, i.e., at strain amplitudes less than 0.60%, the gradual build-up of dislocations during fully reversed cyclic straining coupled with their interaction with the intrinsic microstructural features dispersed through the microstructure results in hardening on a "local" scale, as is evident during the first few cycles of cyclic deformation. When the "local" stress concentration caused by the gradual build-up of dislocations at a microstructural feature, be it (i) the second-phase carbide particle, (ii) the martensite micro-constituent, or (iii) the grain boundary, exceeds a critical value (σ^*), microscopic crack initiation is favored to occur by the following:

(a) Rupture of the hard, brittle, and essentially elastically deforming second-phase carbide particle, and
(b) Cracking at the interface of the martensite micro-constituent with the soft metal matrix.

With continued cyclic straining, numerous such second-phase carbide particles dispersed through the microstructure of this high alloy steel coupled with locations of interfaces of the martensite micro-constituent with the soft metal matrix tend to easily crack on account of their intrinsic brittleness, that is, when the local stress concentration (σ^*) caused by the gradual build-up of dislocations exceeds the strength of the microstructural feature. With continued cyclic straining, the fine microscopic cracks gradually grow in size and eventually link, or coalesce, to form a macroscopic crack. Initiation of one or more macroscopic cracks coupled with the concurrent growth of both the fine microscopic and macroscopic cracks through the microstructure of this high alloy steel results in a gradual decrease in stress-carrying capability before culminating in failure by fracture.

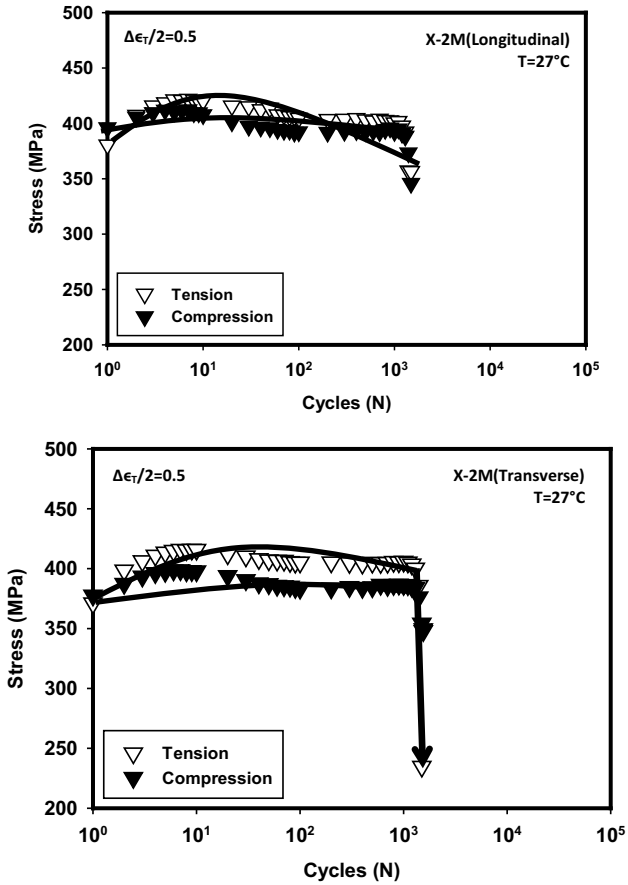

Fig. 7 Variation of tensile stress and compressive stress with cycles for alloy steel X2M for (a) Longitudinal orientation, (b) Transverse Orientation

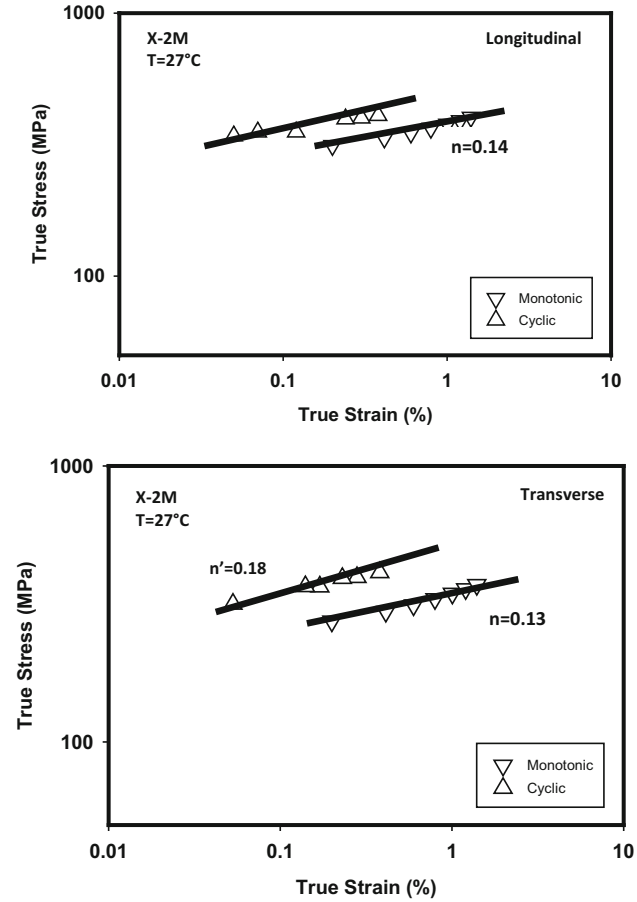

Fig. 8 Comparison of the monotonic and cyclic stress vs. strain curves for alloy steel X2M in the two orientations at room temperature (27 °C)

4.7 Cyclic Stress versus Strain Response

The cyclic stress-strain response is a measure of transient response and is useful for designing microstructures and developing materials having improved cyclic strain resistance. Under fully reversed, total strain amplitude-controlled ($\Delta\varepsilon_T/2$) cyclic straining, the resultant stresses developed in the microstructure of this high alloy steel may be invariant during cycling, that is, they may remain stable, and either increase (harden) or decrease (soften) with continued cycling. Since saturation was not evident for a significant portion of fatigue cycling, the cyclic curve was defined by measuring the strain amplitude and stress amplitude at half-life ($N_f/2$) of the specimen. The cyclic stress-strain curve was obtained by plotting the stabilized stress with plastic strain amplitude [$\Delta\varepsilon_P/2$] (Ref 31-33). The cyclic stress versus strain curve is shown in Fig. 8 and compared with the monotonic stress-strain curve obtained from a simple tension test. This figure reveals that for orientations, longitudinal (L) and transverse (T), the cyclic state is only marginally harder than the monotonic state. The influence of work hardening is important to understanding the role of intrinsic microstructural constituents on cyclic deformation and strain-controlled fatigue response. The influence of the presence of fine second-phase carbide particles in the microstructure can be inferred from this figure. The presence and near uniform distribution of the hard, brittle, and essentially elastically deforming second-phase particles in the microstructure of this alloy steel result in the development of 'localized' stresses in the different regions both at and immediately surrounding the second-phase particle. It is the highly "localized" stresses that contribute, in a small way, to work hardening of the alloy steel during fully reversed cyclic straining. The small concentration of localized stresses also results from the constraints in mechanical deformation arising as a result of noticeable differences in elastic modulus of the hard second-phase particle and the soft ferrite metal matrix. A minor contribution to strength also comes from an increase in dislocation density during cyclic plastic deformation. As the "localized" stresses in the soft metal matrix increase, both from constraints and dislocation multiplication, the volume of microstructure that is plastically deformed increases.

4.8 Interpreting Cyclic Fracture Behavior

At the ambient test temperature (27 °C), fracture surfaces of the samples taken from both the longitudinal (L) and transverse (T) orientations revealed near similar topography at the macroscopic level at both the high cyclic strain amplitude and resultant short fatigue life and low cyclic strain amplitude and concomitant long fatigue life. However, at the fine microscopic level, the fracture surface features were found to vary with cyclic strain amplitude. Representative fractographs of the fatigue fracture surface are shown in Fig. 9, 10, 11, and 12.

4.8.1 Longitudinal (L) Orientation. At total strain amplitude of 0.60% and resultant fatigue life of 1470 cycles, macroscopic fracture of this alloy steel specimen was essentially normal to the far-field stress axis (Fig. 9a). Macroscopic or low magnification, observation in the SEM revealed the region of crack initiation and early microscopic crack growth to be essentially smooth and inlaid with an array of coplanar microscopic cracks and isolated macroscopic crack (Fig. 9b). At higher magnifications, the pockets of flat transgranular regions were inlaid with a random distribution of fine and shallow striations (Fig. 9c). This feature is reminiscent of the occurrence of "localized" microplastic deformation at the fine microscopic level. The short region of stable crack growth revealed a faceted appearance with the grains covered with pockets of well-defined and shallow striations (Fig. 9d). The presence of striations is clearly indicative of the occurrence of microplastic deformation at the local level.

At a lower total strain amplitude of 0.30% and resultant fatigue life of 5526 cycles, overall morphology was normal to the far-field stress axis revealing two distinct regions representing fatigue and overload (Fig. 10a). The region of early crack growth when carefully observed at higher magnifications revealed an observable population of fine microscopic cracks along with pockets of striations. These features are reminiscent of both brittle and ductile mechanisms occurring at the fine microscopic level (Fig. 10b). The transition region between fatigue and overload was rough at the microscopic level comprising of a population of fine microscopic voids of varying size intermingled with macroscopic cracks. These features are indicative of both ductile and brittle mechanisms at the fine microscopic level (Fig. 10c). The region of overload was rough at the fine microscopic level comprising of voids of varying size intermingled with shallow dimples and void coalescence to

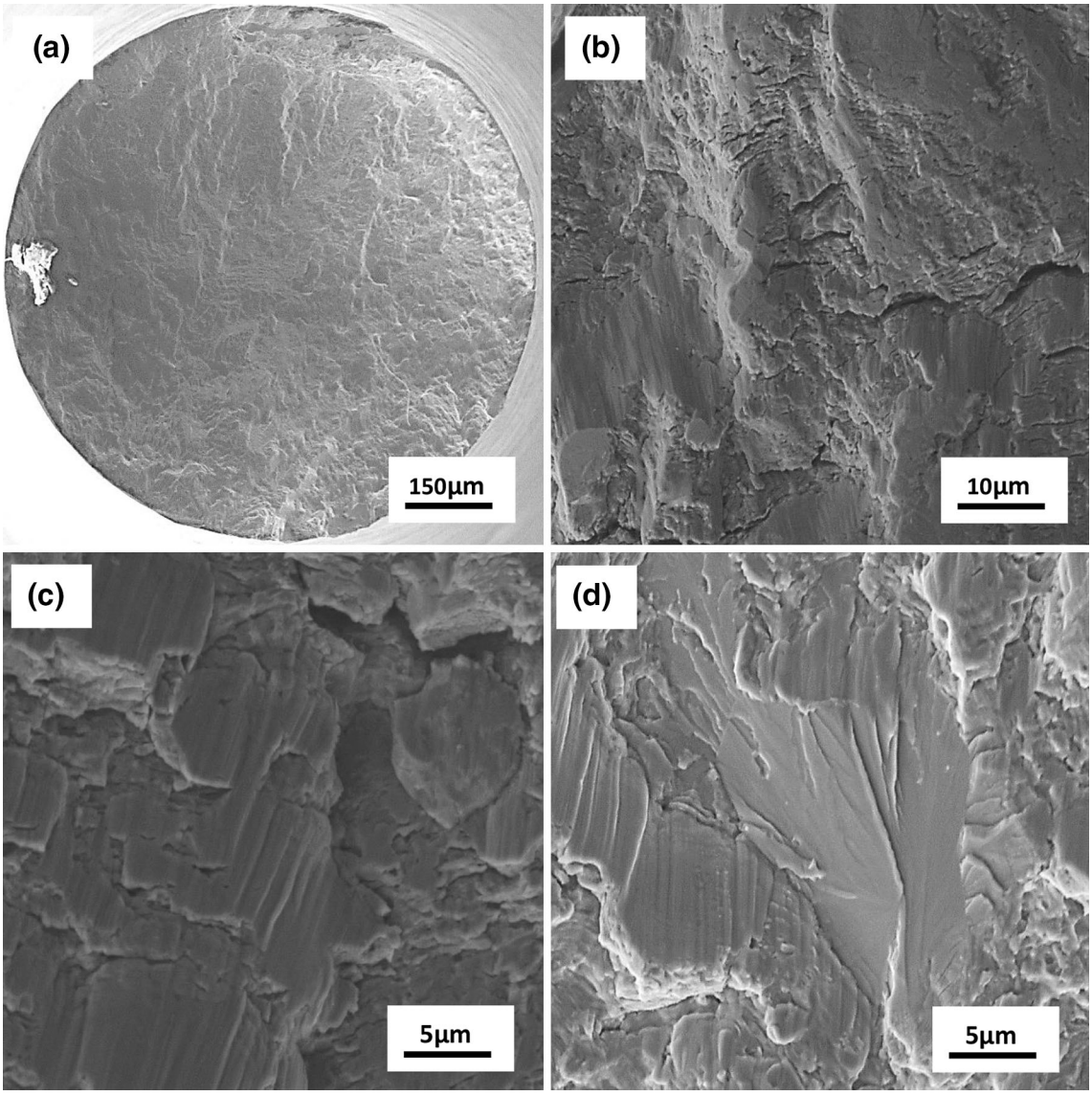

Fig. 9 Scanning electron micrographs of the fatigue fracture surface of alloy steel X2M sample, taken from longitudinal orientation, cyclically deformed at a strain amplitude of 0.6%, with a fatigue life of 1470 cycles, showing (a) Overall morphology of failure (b) Region of stable crack growth flat and inlaid with an array of fine microscopic and macroscopic cracks (c) Region of stable crack growth showing pockets of fine striations (d) Region of stable crack growth prior to overload showing array of well-defined striations

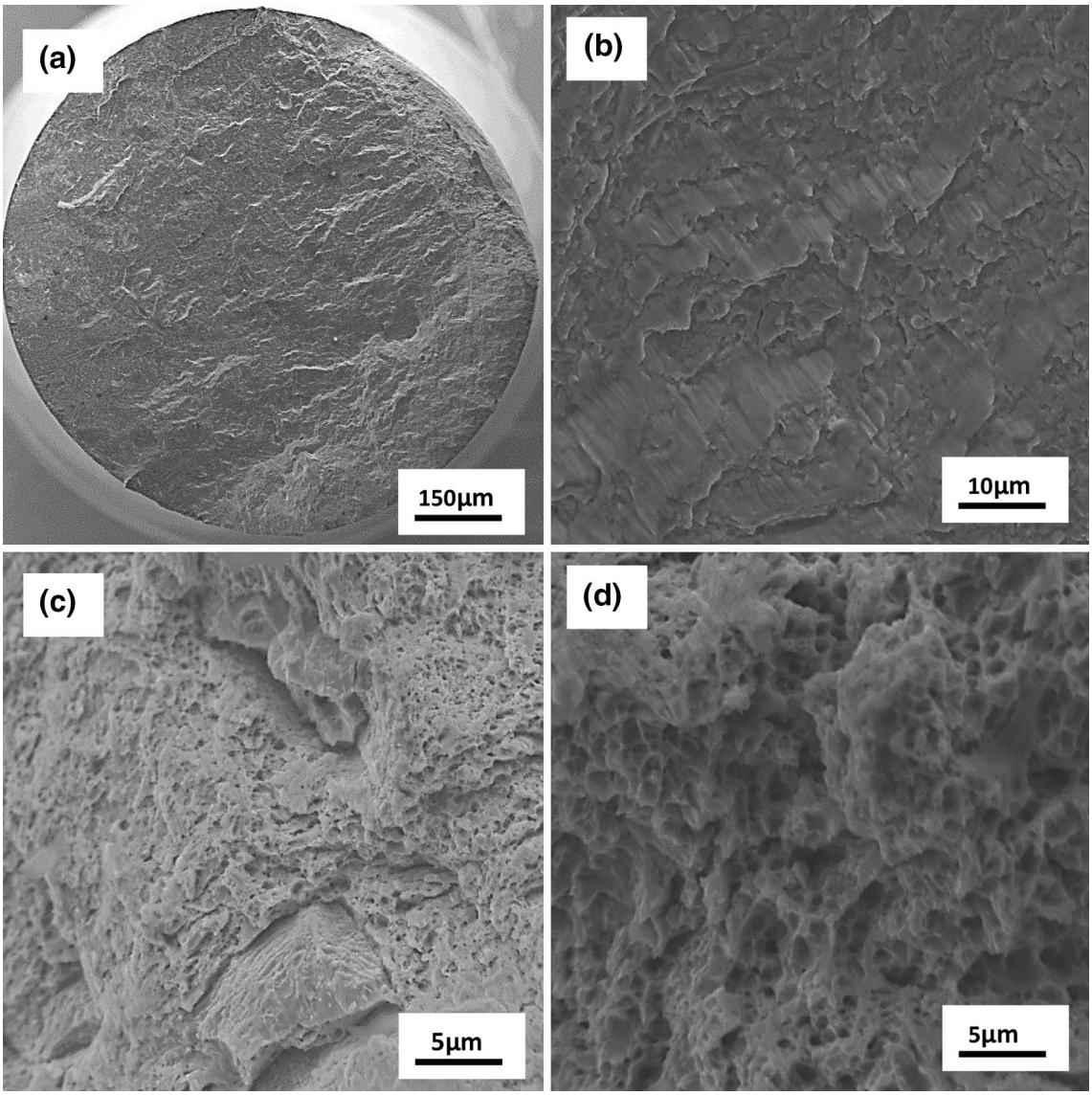

Fig. 10 Scanning electron micrographs of the fatigue fracture surface of alloy steel X2M sample, taken from longitudinal orientation, cyclically deformed at a strain amplitude of 0.3% with a fatigue life of 5526 cycles, showing (a) Overall morphology of failure. (b) Region of early crack growth flat and inlaid with striations and an array of coplanar microscopic cracks (c) Region of unstable crack growth prior to overload showing a combination of cracks, fine microscopic voids and shallow dimples (d) Voids of varying size, void coalescence to form a fine microscopic crack and shallow dimples in the region of overload

result in the formation and presence of fine microscopic cracks (Fig. 10d).

4.8.2 Transverse (T) Orientation. At a total strain amplitude of 0.50% and resultant fatigue life of 1550 cycles, macroscopic fracture of this high alloy steel test specimen was rough and essentially normal to the far-field stress axis (Fig. 11a). Macroscopic, or low magnification, observation in the SEM revealed the region representing crack initiation and early microscopic crack growth to be flat and inlaid with a sizeable number of randomly oriented short and fine microscopic cracks (Fig. 11b). High magnification observation of the fracture surface revealed an array of coplanar microscopic cracks and non-linear macroscopic cracking (Fig. 11c). The presence of distinct striations was not easily evident on the surface of this alloy steel specimen even at high magnifications. The region of overload was rough and contained fine microscopic voids of varying size intermingled with pockets of shallow dimples and fine microscopic cracks. These features are reminiscent of the "locally" occurring ductile and brittle failure mechanisms.

At a lower cyclic strain amplitude of 0.36% and resultant fatigue life of 3902 cycles, overall fracture was rough at the fine microscopic level and revealed a small region representing fatigue and a sizeable region representative of unstable crack growth and overload (Fig. 12a). The region representing fatigue and early crack growth was flat, smooth, and inlaid with an observable number of fine microscopic and macroscopic cracks (Fig. 12b). The region of stable crack growth was short, and high magnification observation revealed well-defined striations reminiscent of "locally" occurring microplastic deformation (Fig. 12c). The region of tensile overload was rough at the fine microscopic level (Fig. 12d) and did contain a sizeable number of microscopic voids intermingled with

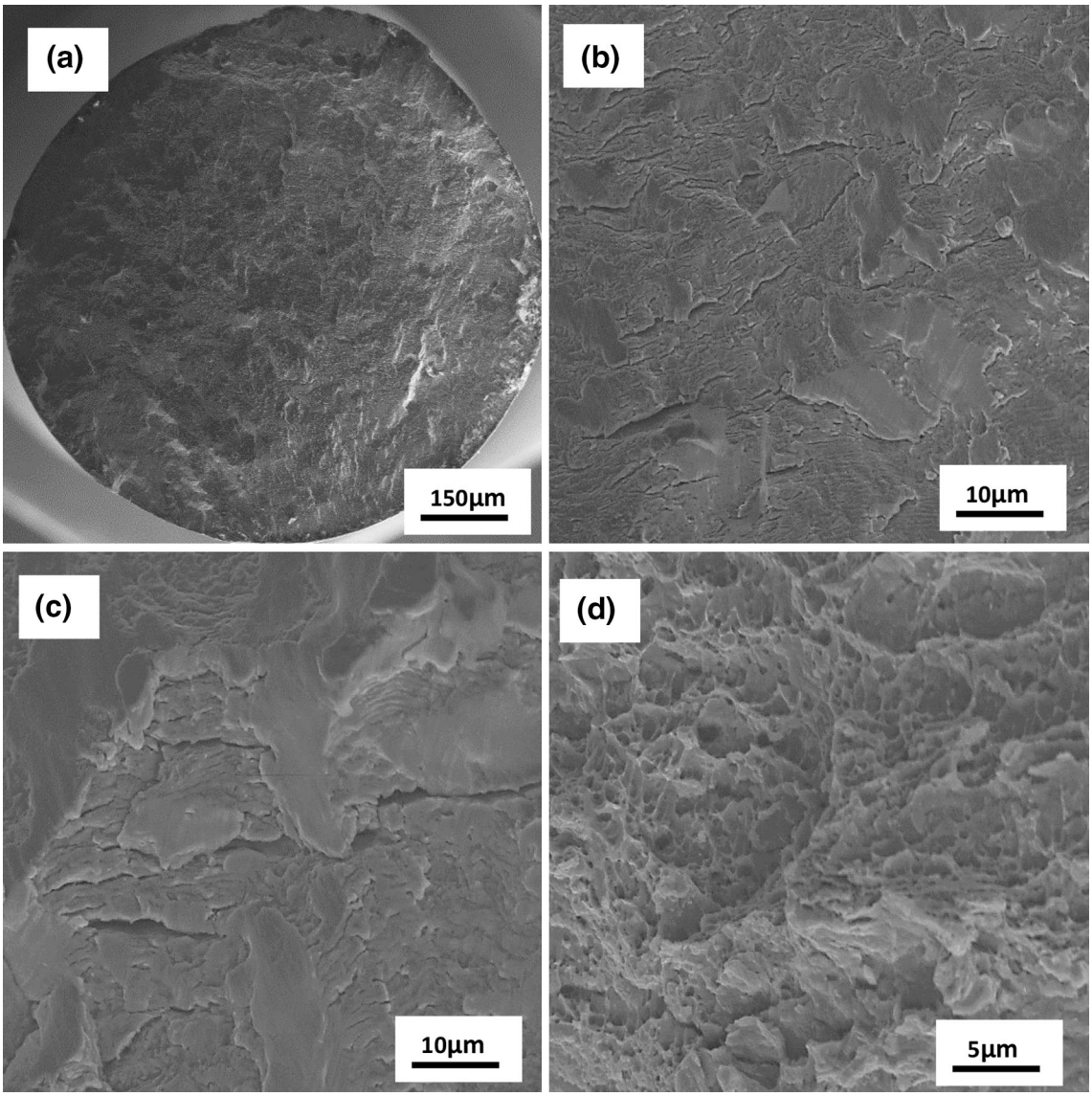

Fig. 11 Scanning electron micrographs of the fatigue fracture surface of alloy steel X2M sample, taken from transverse orientation, cyclically deformed at a strain amplitude of 0.5%, with a fatigue life of 1550 cycles, showing (a) Overall morphology of failure (b) Region of early microscopic crack growth showing numerous fine microscopic cracks (c) Region of unstable crack growth prior to overload (d) A noticeable population of dimples, microscopic voids, and microscopic cracks covering the overload fracture surface

shallow pockets of dimples and macroscopic cracks. These features are indicative of the occurrence of both ductile and brittle mechanisms at the fine microscopic level. Half of the void is the dimple, observed in sizeable number, on the fatigue fracture surfaces of both the longitudinal (L) and transverse (T) samples.

4.8.3 Microscopic Mechanisms Governing Cyclic Fracture. The key mechanisms controlling fracture of this high alloy steel when cyclically deformed at ambient temperature (27 °C) can be summarized as

(i) A noticeable mismatch in strain carrying capability between the soft, ductile, and plastically deforming alloy steel matrix and the hard, brittle, and essentially elastically deforming microstructural feature, be it a coarse second-phase carbide particle or the martensite micro-constituent.

(ii) This causes a large concentration of stress to occur at the second-phase carbide particle or the martensite micro-constituent, thereby enabling cracking to easily occur at its interface with the soft metal matrix. The ease of occurrence of fine microscopic cracks suggests that 'local' plastic strain dominates in regions of the hard, brittle, and essentially elastically deforming microstructural feature.

Cracking of both the martensite micro-constituent and the coarse second-phase carbide particles occurred normal to the far-field stress axis. The occurrence of plastic strain inhomogeneity at the fine microscopic level within the grains and exacerbated by the presence of coarse second-phase carbide particles is believed to be responsible for the traces of intergranular cracking observed.

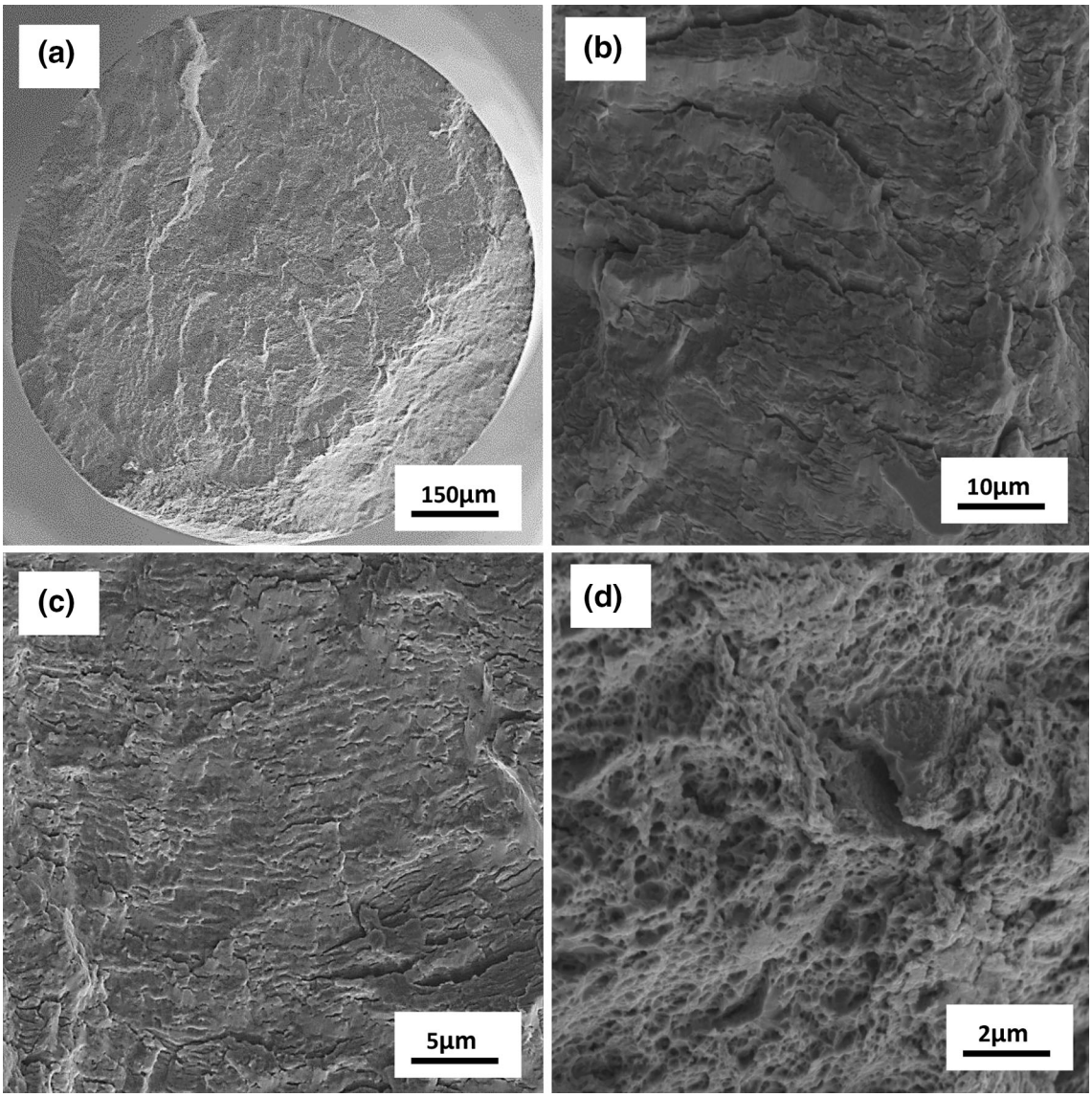

Fig. 12 Scanning electron micrographs of the fatigue fracture surface of alloy steel X2M sample, taken from transverse orientation, that was cyclically deformed at strain amplitude of 0.36%, with a fatigue life of 3902 cycles, showing (a) Overall morphology of failure (b) Region of early microscopic crack growth showing an array of fine microscopic cracks (c) Numerous striations in the region of stable crack growth (d) Healthy dispersion of dimples, intermingled with microscopic voids and fine microscopic cracks

5. Conclusions

Based on the results of an investigation aimed at understanding the strain-controlled low-cycle fatigue response and resultant fracture behavior of this high-strength high alloy steel, i.e., X2M, following are the key findings.

1. Optical microstructure of this high-strength steel revealed a combination of alloy-rich, carbon-rich, and carbon-depleted regions. A higher carbon and alloy content in this steel resulted in a greater volume fraction of second-phase particles and the micro-constituent martensite in the alloy-rich and carbon-rich regions.
2. The elastic modulus of this alloy steel was noticeably different in the two orientations longitudinal (L) and transverse (T). The modulus in the transverse direction (150 GPa) was fourteen percent lower than the elastic modulus in longitudinal direction (175 GPa). The yield strength in the longitudinal (L) orientation [371 MPa] was forty percent more than in the transverse orientation [264 MPa]. The ultimate tensile strength in the longitudinal orientation [638 MPa] is twenty percent higher than in the transverse orientation [523 MPa]. The ductility quantified by elongation over 0.5 inch (12.7 mm) gage length was observably higher in the transverse (T) orientation than in the longitudinal (L) orientation. The reduction in test specimen cross-section area was higher in the transverse (T) orientation (60%). The observed higher ductility is consistent with the lower yield strength and tensile strength in the transverse orientation.
3. This high-strength alloy steel exhibited a linear trend for the variation of elastic strain amplitude ($\Delta\varepsilon_e/2$) with reversals-to-failure ($2N_f$), and plastic strain amplitude ($\Delta\varepsilon_P/2$) with reversals-to-failure ($2N_f$).

4. 4. At the high, low, and intermediate cyclic strain amplitudes, stress response of this high-strength alloy steel revealed initial hardening during the first few cycles of fully reversed cyclic straining followed by gradual softening for most of fatigue life at both the lower and intermediate strain amplitudes. However, at the higher strain amplitudes, the softening was significant before culminating in rapid softening prior to the occurrence of failure by fracture.
5. Fracture morphology was the same at the macroscopic level over the entire range of cyclic strain amplitudes examined. However, at the fine microscopic level, this high alloy steel test specimen that was deformed at the higher cyclic strain amplitude revealed fracture to be essentially ductile with features reminiscent of predominantly "locally" ductile mechanisms. At the lower strain amplitudes, microscopic observations of the fracture surface at the higher allowable magnifications of the SEM revealed features to be reminiscent of both "locally" ductile and brittle failure mechanisms.

References

1. G.R. Speich, D.S. Dabkowski, and L.F. Porter, Strength and Toughness of Fe-10Ni Alloys Containing C, Cr, Mo, and Co, *Metall. Trans.*, 1973, **4**, p 303–315
2. W.E. Wood, Discussion of "Evaluation of Toughness in AISI, 4340 Alloy Steel Austenitized at Low and High Temperatures, *Metall. Trans.*, 1977, **8A**, p 1195–1199
3. F. Zia Ebrahimi and G. Krauss, The Evaluation of Tempered Martensite Embrittlement in 4130 STEEL by Instrumented Charpy V-Notch Testing, *Metall. Trans.*, 1983, **14A**, p 1109–1119
4. G.B. Olson, M. Azrin, E.S. Wright, *Innovations in Ultrahigh Strength Steel Technology* (Editors), US Army Materials Technology Laboratory, Watertown, MA, 1990, pp. 89–109
5. G.Y. Lai, On High Fracture Toughness of Coarse-Grained AISI, 4130 Steel, *Mater. Sci. Eng.*, 1975, **19**, p 153–156
6. R.O. Ritchie and R.M. Horn, Further Considerations on the Inconsistency in Toughness Evaluation of AISI, 4340 Steel Austenitized at Increasing Temperatures, *Metall. Trans.*, 1978, **9A**, p 331–341
7. B.V. Narasimha Rao and G. Thomas, Structure-Property Relations and the Design of Fe-4Cr-C Base Structural Steels for High Strength and Toughness, *Metall. Trans.*, 1980, **11A**, p 441–457
8. F. Zia Ebrahimi, Mechanisms of Tempered Martensite Embrittlement in Medium—Carbon Steels", *Acta Metall.*, 1984, **32**, p 1767–1778
9. W.M. Garrison, A Microstructural Interpretation of the Fracture Strain and Characteristics Fracture Distance, *Scripta Metall.*, 1984, **18**, p 583–586
10. W.M. Garrison, The Effect of Silicon and Nickel Additions on the Sulfide Spacing and Fracture Toughness of a 0.4 Carbon Low Alloy Steel, *Metall. Trans.*, 1986, **17A**, p 669–678
11. W.M. Garrison, Jr, and N.R. Moody, The Influence of Inclusion Spacing and Microstructure on the Fracture Toughness of the Secondary Hardening Steel AF 1410, *Metall. Trans.*, 1987, **18A**, p 1257–1263
12. B.C. Kim, S. Lee, D.Y. Lee, and N.J. Kim, In Situ Fracture Observations on Tempered Martensite Embrittlement in an AlSl 4340 Steel, *Metall. Trans.*, 1991, **22A**, p 1889–1892
13. M.A. Linanza, J.L. Romero, J.M. Rodriguez-Illabe, and J.J. Urcola, Influence of the Microstructure on the Fracture Toughness and Fracture Mechanisms of Forging Steels Micro Alloyed with Titanium with Ferrite-Pearlite Structures, *Scripta Metall. Mater.*, 1993, **29**, p 451–456
14. M.A. Linanza, J.L. Romero, J.M. Rodriguez-Illabe, and J.J. Urcola, Cleavage Fracture of Microalloyed Forging Steels, *Scripta Metall. Mater.*, 1995, **32**, p 395–400
15. M.J. Leap and J.C. Wingert, The Effects of Grain-Refining Precipitates on the Development of Toughness in 4340 Steel, *Metall. Mater. Trans.*, 1999, **30A**, p 93–114
16. R. Branco, J.D. Costa, F.V. Antunes, Low-cycle Fatigue Behavior of 34CrNiMo6 High Strength Steel, *Theo. Appl. Fract. Mech.*, 2012, **58**(1),p 28–34, ISSN 0167-8442
17. C. Zhang, X. Song, P. Lu, X. Hu, Effect of Microstructure on Mechanical Properties in Weld-Repaired High Strength Low Alloy Steel, *Mater. Des.* 2012, **36**, p 233–242, ISSN 0261-3069
18. Y.-R. Luo, C.-X. Huang, R.-H. Tian, Q.-Y. Wang, Effects of Strain Rate on Low Cycle Fatigue Behaviors of High-Strength Structural Steel, J. Iron Steel Res. Int., 2013 **20** 7), p 50–56, ISSN 1006-706X
19. R.J. Cunningham, (1975), *Process for Carburizing High Alloy Steels*, U.S. Patent Number 3,885,995
20. R.J. Cunningham (1974), Boeing-Vertol Division of Boeing Company "Steel (X2M) Transmission Gear Material Evaluation, Test Results and Final Report, U.S. Government Contract No. DAAJ01 70-C-0840
21. B.L. Averbach, P.K. Bingzhe Lou, R.E. Pearson, Fairchild, and E.N. Bamberger, Fatigue Crack Propagation in Carburized High Alloy Bearing Steels, *Metall. Trans.*, 1985, **16A**, p 1253–1259
22. B.L. Averbach, P.K. Bingzhe Lou, R.E. Pearson, Fairchild, and E.N. Bamberger, Fatigue Crack Propagation in Carburized X2M Steel, *Metall. Trans.*, 1985, **16A**, p 1267–1271
23. D.P. Davies and S.L. Jenkins, Influence of Stress and Environment on the Fatigue Strength and Failure Characteristics of Case Carburized Low Alloy Steels for Aerospace Applications, *Int. J. Fatigue*, 2012, **44**, p 234–244
24. ASTM E-8-06: *Tensile Testing of Metallic Materials*, American Society of Testing and Materials, Philadelphia, PA, 2006
25. T.S. Srivatsan, A.S. Naruka, B.G. Ravi, T.S. Sudarshan, M. Petraroli, and L. Riester, The Microstructure and Properties of Molybdenum-Copper Composite Metal Samples Consolidated by Plasma Pressure Compaction, *Powder Metall.*, 2002, **45**(3), p 255–260(6)
26. T.S. Srivatsan, B.G. Ravi, A.S. Naruka, L. Riester, L. Yoo, and T.S. Sudarshan, Microstructure and Hardness of Copper Powders Consolidated by Plasma Pressure Compaction, *J. Mater. Eng. Perform.*, 2001, **10**(4), p 449–455
27. T.S. Srivatsan, B.G. Ravi, A.S. Naruka, L. Riester, S. Yoo, and T.S. Sudarshan, A Study of Microstructure and Hardness of Bulk Copper Samples Obtained by Consolidating Nanocrystalline Powders Using Plasma Pressure Compaction, *Mater. Sci.Eng. A*, 2001, **A311**, p 22–27
28. L.F. Coffin, Jr., and J.F. Travernelli, The Cyclic Straining and Fatigue of Metals, *Transactions TMS-AIME*, 1959, **215**(5), p 794–806
29. S.S. Manson, and M.H. Hirschberg, "*Fatigue Behavior of Strain Cycling in the Low and Intermediate Cycle Range*," 10th Sagamore Army Materials Research Conference, Raquette Lake, NY, August 13–16, 1963
30. T.H. Topper, B.I. Sandor, and J. Morrow, Cumulative Fatigue Damage Under Strain Control, *J. Mater.*, 1969, **4**, p 189–199
31. S.S. Manson, NASA Technical Note, National Aeronautics and Space Administration, 1954, p. 2933–2940
32. B. Sandor, *I: Fundamentals of Cyclic Stress and Strain*, University of Wisconsin Press, Madison, 1972
33. E.A. Starke, Jr, and G. Lutjering, "*Cyclic Plastic Deformation and Microstructure"*, in Fatigue and Microstructure (edited: M. Meshii) American Society for Metals, Metals Park, Ohio, USA, 1979, p. 205–240